Crustal anisotropy in a subduction zone forearc: Northern Cascadia

by

Gian Matharu

B.Sc. (Hons), The University of British Columbia, 2011

A THESIS SUBMITTED IN PARTIAL FULFILLMENT OF
THE REQUIREMENTS FOR THE DEGREE OF

MASTER OF SCIENCE

in

The Faculty of Graduate and Postdoctoral Studies

(Geophysics)

THE UNIVERSITY OF BRITISH COLUMBIA

(Vancouver)

April 2014

Abstract

S-wave splitting analyses using high signal-to-noise ratio low frequency earthquake (LFE) templates at 3-component stations across southern Vancouver Island (SVI) and northern Washington indicate the presence of a heterogeneous distribution of crustal anisotropy in the North American plate. For SVI, we investigate the contribution to anisotropy from the Leech River Complex (LRC), an allochthonous terrane comprised of strongly foliated greenschist facies phyllites and amphibolite facies schists with steeply dipping foliations striking E-W. On SVI, estimates of initial S-wave polarization direction are consistent with predictions from radiation patterns generated by LFE focal mechanisms, providing corroboration for thrust mechanisms at the plate boundary. Fast directions across mainland SVI are subparallel to the dominant foliation direction in the LRC. Increases in depth normalized delay times from east to west, combined with small-scale azimuthal variations in fast directions suggest a heterogeneous distribution of anisotropy. We test azimuthally anisotropic LRC models based upon analyses of geological fabric and geometrically constrained by reflection studies, through forward modeling using 3D spectral element method (SEM) simulations. The preferred model of a north/northeast shallowly dipping wedge of LRC material with varying orientations of anisotropy terminating at mid crustal levels is able to recreate mean and azimuthal variations in fast directions along with variations in delay times, thereby supporting the hypothesis of the LRC as a primary contributor to crustal anisotropy beneath SVI. For select stations where anisotropic LRC models do not recreate observations, fast directions are subparallel to local estimates of maximal compressive horizontal stress, suggesting fluid-filled cracks could be a source of anisotropy. We refute the idea that anisotropy along mainland SVI is primarily due to stress related cracks as has been suggested by prior studies. Fast directions at stations on northern Washington exhibit variations with azimuth and incidence angle suggesting complex anisotropy interpreted as due to a combination of cracks and preferred mineral orientation of metamorphosed slates of the Olympic core rocks. These slates may also underlay stations on SVI and represent another source of anisotropy.

Preface

The content of this thesis is original and does not include text from prior publications. This thesis is based on the analysis of process data obtained by *Bostock et al.* [10], *Royer and Bostock* [41] as detailed in chapter 2. The analyses in chapter 3 and 5 follow well established techniques in seismology but present original results. I conducted model testing in chapter 4 with guidance from collaborator J. Tromp regarding proper model design implementation. Chapter 4 uses open source software SPECFEM3D to perform the modeling. Chapters 6 and 7 are based on my original analyses that were guided through discussions with supervisors M. Bostock and N.I. Christensen.

Table of Contents

List of Tables

List of Figures

Acknowledgements

Foremost I would like to thank my supervisor Michael Bostock for his generosity, patience and unwavering support. His expertise and experience in the field have been invaluable for the completion of this thesis along with my growth as an aspiring researcher. I am also grateful to Nik Christensen for his multifaceted insight into the interpretation of results along with his inspiring enthusiasm. I would also like to thank Nik, Ron Clowes and Felix Herrmann for having served on my supervisory committee. I am thankful to Jeroen Tromp and his group at Princeton University for accommodating me and exposing me to the field of computational seismology, their insight into modeling techniques was essential. I express my gratitude to Kumar Ramachandran for providing us with his tomographic model of Vancouver Island allowing us to improve our modeling efforts.

Chapter 1

Introduction

The discovery of low frequency earthquakes (LFEs) as a component of tectonic tremor presents a novel and unexplored means of studying local subduction zone structure. At the time that LFEs were originally discovered in SW Japan as discrete events on seismograms, their relation to episodic tremor and slip (ETS) had not yet been ascertained [6, 38]. Later work using network correlation methods showed that tectonic tremor can be considered as a superposition of many LFEs undergoing repeated ruptures at a range of different earthquake locations [44]. Correlation methods have been used to identify LFE events among tremor signals in both SW Japan [14, 43] and Cascadia [10, 14]. LFEs are small earthquakes ($M_w \approx 2.0$) with characteristic frequencies of 1-10 Hz that result from shear slip at the plate boundary [31, 41, 44]. The predominantly horizontal motion of the rupture leads to strong S-wave arrivals on horizontal component seismograms at small epicentral distances. The consistent mechanism and local nature of LFEs suggest their use as a new seismic source to image regional subduction zone structure. In the Cascadia subduction zone where regular seismicity is relatively scarce, LFEs present a potentially valuable imaging tool.

The North American plate overrides the subducting Juan de Fuca plate in Cascadia and exhibits crustal anisotropy that has been documented in earlier S-wave splitting analyses of southern Vancouver Island (SVI) [4, 9, 15, 25]. The origins of crustal anisotropy are often disputed but are generally ascribed to either stress-aligned fluid-saturated fractures [e.g. 23, 24] or the preferred mineral orientation of rocks [e.g. 16, 17]; both have been cited as explanations for anisotropy observed on SVI. Schematic diagrams illustrating the two types of anisotropy are shown in figure 1.1. We seek to provide further insight into the cause of anisotropy beneath SVI using LFEs. In Cascadia, LFEs generate waves that propagate upwards through the forearc crust of the North American plate. Consequently, any anisotropy observed at nearby stations can be attributed directly to local crustal anisotropy as the observed waveforms have not encountered any contribution from mantle structure.

Chapters 2-4 of this study focus solely on SVI for which the analysis is divided into two components. In the first part (sections 2-3), we outline and conduct a splitting analysis of LFE data, present observations and compare them with previous studies of crustal anisotropy in the region. We then expand on the work of *Bostock and Christensen* [9] by developing anisotropic models for SVI and computing synthetic seismograms using a spectral element method (section 4). We continue to develop the hypothesis that crustal anisotropy in the region is primarily influenced by mineral orientation of metamorphic rocks from the Leech River Complex (LRC), as opposed to stress-aligned fluid-saturated cracks. In section 5 we include a less extensive splitting analysis for LFE data from northern Washington, an extension that permits a more comprehensive interpretation of anisotropy in the northern Cascadia forearc crust.

1.1 Elastic anisotropy

Elastic anisotropy refers to the property of a medium whereby the velocity of a seismic wave depends on its direction of propagation and polarization. As a linearly polarized S-wave enters an anisotropic medium it is usually split into two quasi S-waves, qS_1, qS_2 that are orthogonal, and have polarization directions determined by the elastic properties of the medium. A commonly assumed form of anisotropy is transverse isotropy, which has one axis of symmetry. If the propagation direction of an incoming S-wave lies along the axis of symmetry, the S-wave is not split nor is the vibration direction altered. For other directions of propagation the S-wave is split into two waves with different velocities (figure 1.1). The velocity difference results in a delay time δt between the qS_1 and qS_2 waves, the magnitude of which depends on the strength of anisotropy. More specifically, the integrated time delay is dependent on the difference between fast and slow wavespeeds along with the extent of the anisotropic material. In order to observe and characterize shear wave splitting, the delay time δt and the fast polarization direction ϕ, are typically measured. Splitting measurements can be used to map anisotropy and subsequently can be related to past or present deformation processes.

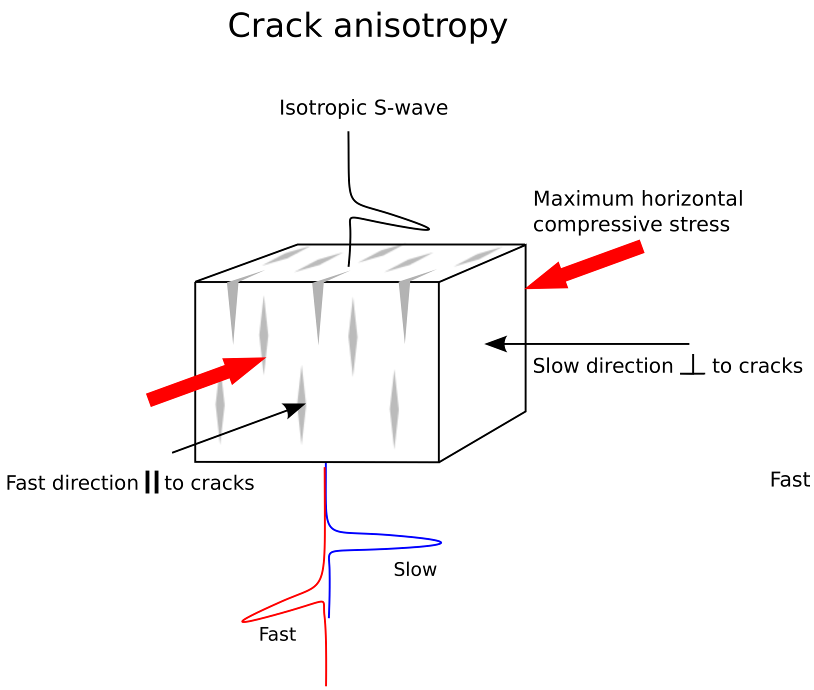

Figure 1.1: S-wave splitting schematic diagram. Two main sources of crustal anisotropy, cracks and preferred mineral orientation, are illustrated with fast directions.

Chapter 2

LFE Templates

The LFE templates [10, 41] used in this study were generated using network correlation methods [13, 43] on ETS episodes occurring in 2003 to 2013 along SVI over a set of 7 anchor stations. A group of initial LFE templates were subject to a network cross correlation over an expanded range of stations (figure 2.1) in an iterative manner that allowed for improvement to the signal-to-noise ratio level (SNR) of LFE template waveforms. For more details on the LFE template acquisition in Cascadia, the reader is referred to *Bostock et al.* [10] and *Royer and Bostock* [41].

LFE template waveforms, like tremor, are bandlimited and show characteristic frequencies of 1-10 Hz on SVI. When an entire set of templates at an individual station is plotted in a seismogram section, there is considerable uniformity across the section, indicative of a simple and consistent source mechanism. These observations were interpreted as an indication that LFE template waveforms on SVI could be considered as empirical Green's functions [10]. The dipolar pulse on far-field particle velocity seismograms is representative of a point source characterized by a step function time dependence in displacement (figure 2.2).

LFE epicenters on SVI are distributed in a band approximately constrained by the 25 and 37 km plate boundary depth contours (figure 2.3) [2], a region where regular seismicity is scarce. The LFE locations show some degree of segregation with local crustal and intraslab earthquakes (figure 2.3) [10]. Similar to LFEs in Japan [43], LFEs in Cascadia have been located near the top of a high V_p/V_s, low S velocity zone [10], which in Cascadia is inferred to be the upper oceanic crust [8, 30]. Waveform modeling of several LFE templates requires LFEs to be located within the upper 1 km of the low velocity zone [39].

As preprocessing steps for the splitting analysis, LFE template waveforms are bandpass filtered between 1 and 8 Hz after which windows are manually selected around S-wave arrivals and subjected to a cosine taper. In the event no clear arrival is apparent across any component, the window is removed from further analysis. Given the station and event distribution, most LFEs represent small incidence angles due to steep raypaths; however, some source receiver geometries are wide enough that effects of the free surface may become important. To mitigate such effects we apply a 1-D wavefield decomposition that takes radial-transverse-vertical component (u_R, u_T, u_Z) seismograms and transforms them into upgoing P-SV-SH waveforms [32]. This transformation requires estimates of the horizontal slowness (p), near surface velocities (α, β) and density (ρ).

$$\begin{bmatrix} P \\ SV \\ SH \end{bmatrix} = \begin{bmatrix} p\beta^2/\alpha & 0 & \frac{\beta^2 p^2 - \frac{1}{2}}{\alpha q_\alpha} \\ \frac{\frac{1}{2} - \beta^2 p^2}{\beta q_\beta} & 0 & p\beta \\ 0 & \frac{1}{2} & 0 \end{bmatrix} \begin{bmatrix} U_R \\ U_T \\ U_Z \end{bmatrix} \tag{2.1}$$

where $q_\alpha = \sqrt{\alpha^{-2} - p^2}$ and $q_\beta = \sqrt{\beta^{-2} - p^2}$. We exclude seismograms that have incidence angles greater than a critical angle, $\theta_c = \sin^{-1}(\beta/\alpha)$. For surface velocities in northern Cascadia this corresponds to $\theta_c \approx 35°$. Beyond θ_c, surface reflection coefficients become complex, leading to phase rotations that preclude a standard splitting analysis. This criterion coincides with the "S-wave window" desirable for S-wave splitting analysis [7].

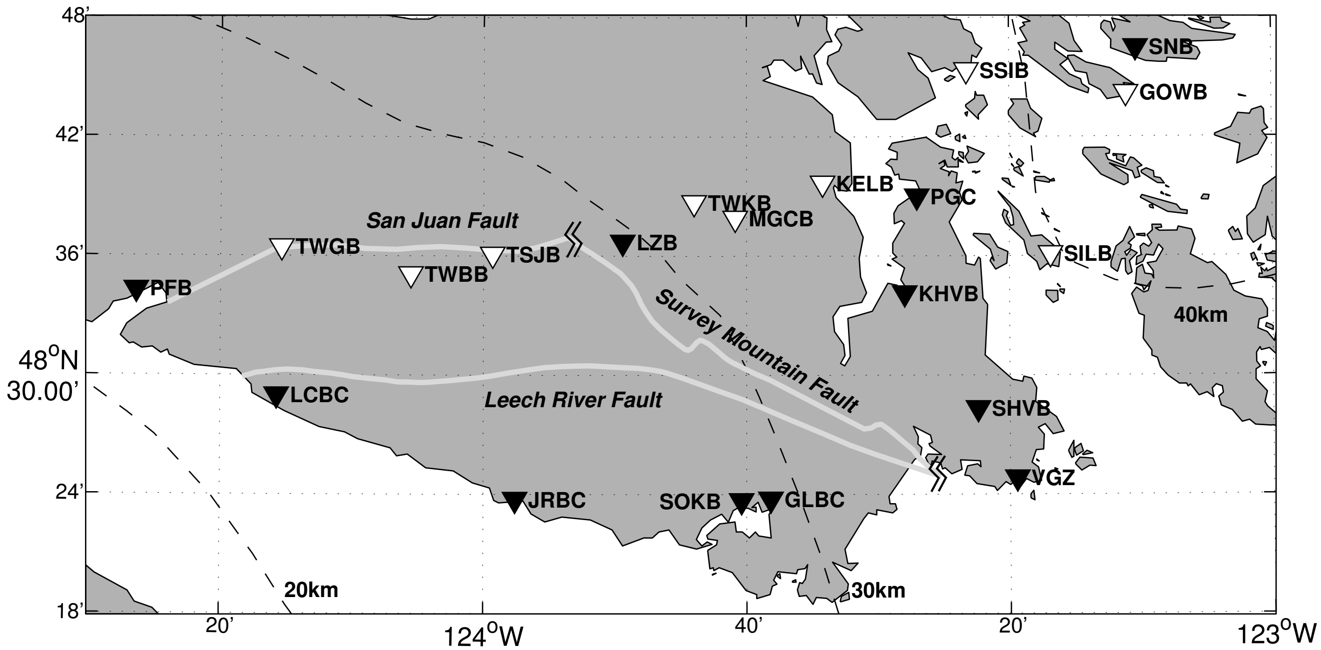

Figure 2.1: Map of SVI stations employed in this study. POLARIS-BC stations are represented by white triangles with remaining stations displayed as black triangles. Light grey contour illustrates the LRC boundary, with the bounding faults labelled and divided by double zig-zag lines. Dashed lines represent 20, 30 and 40 km depth contours for the subducting Juan de Fuca plate [2].

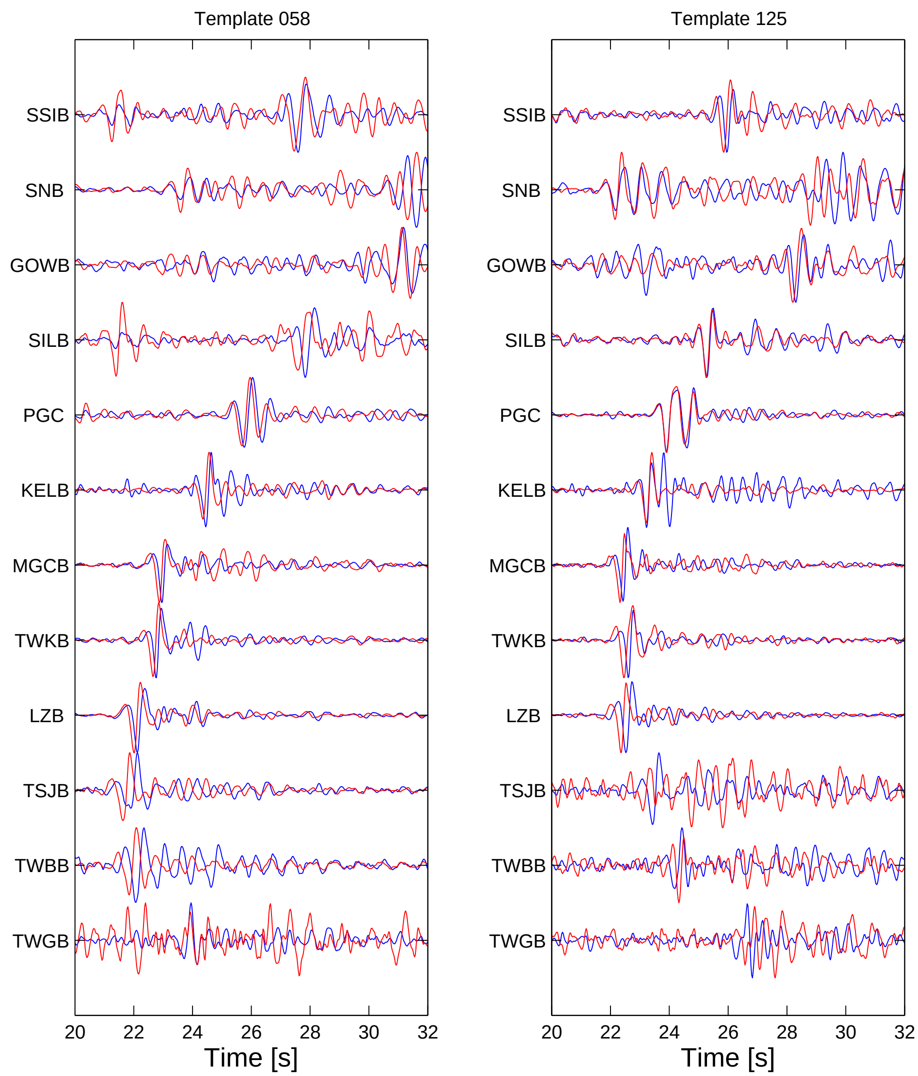

Figure 2.2: Horizontal component sections of two SVI LFE templates displaying north (blue) and east (red) components. Clear splitting can be seen at certain stations (e.g. TWKB, MGCB, LZB) whereas others show strong waveform distortions (e.g. TWBB, TWGB).

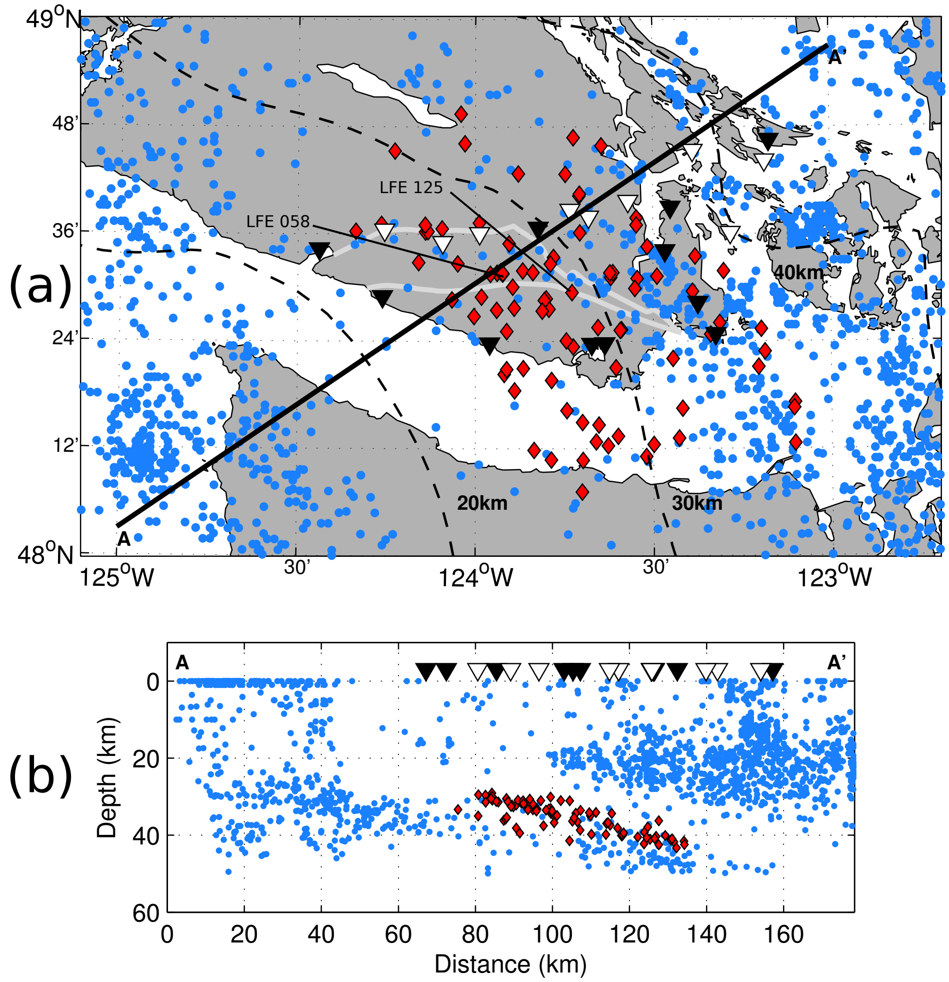

Figure 2.3: Map of local SVI earthquake epicenters and stations. LFEs are shown as red diamonds and crustal/instraslab earthquakes ($M_w > 1.0$, event depth < 50 km) are shown as blue dots. LRC boundary is shown in light grey. Depth profile of seismicity along line AA' is shown in (b).

Chapter 3

Splitting Analysis

3.1 Methodology

We perform a standard, two-parameter S-wave splitting analysis that searches for δt and ϕ that minimize the second eigenvalue λ_2 of the covariance matrix for the shifted and rotated horizontal component seismograms [45]. This procedure serves to maximize the linearity of the particle motion thereby identifying the original, unsplit S-waveform, assuming that the medium is adequately modeled by constant anisotropy. The eigenvector corresponding to the largest eigenvalue of the corrected covariance matrix is used to obtain an estimate for the initial polarization direction ϕ_0. Figure 3.1 shows stages of the splitting analysis at station TWKB for LFE template 002.

The standard splitting analysis is susceptible to null measurements that occur when there is an inherent lack of anisotropy along the raypath, when a wave propagates along the axis of symmetry in a transversely isotropic medium or when the initial polarization direction is coincident with the fast or slow direction. For a parameter combination (ϕ_m, δt_m) that minimizes $\lambda_2(\phi,\ \delta t)$ of the splitting analysis (figure 3.1c), there are three scenarios under which the measurement is deemed null:

1) If ϕ_0, $\phi_0+\frac{\pi}{2}$ or $\delta t = 0$ lie within the 95% confidence level (τ) of $\lambda_2(\phi_m$,

δt_m)

2) $\delta t_m > \delta t_{max}$, where δt_{max} is an upper limit imposed based upon realistic expectations for measurements in the region (set at 0.3 s) [e.g. 4, 9, 15, 25].

3) Both ϕ_0 or $\phi_0 + \frac{\pi}{2}$ and $\delta t = 0$ lie within 2τ of $\lambda_2(\phi_m, \delta t_m)$.

The final criterion was chosen due to empirical evidence that showed measurements falling into this category consistently failed to follow expected splitting behaviour. The 95% confidence levels are computed assuming an F-distribution. Hereafter, usage of ϕ and δt refers exclusively to solutions of the splitting analysis, ϕ_m and δt_m respectively.

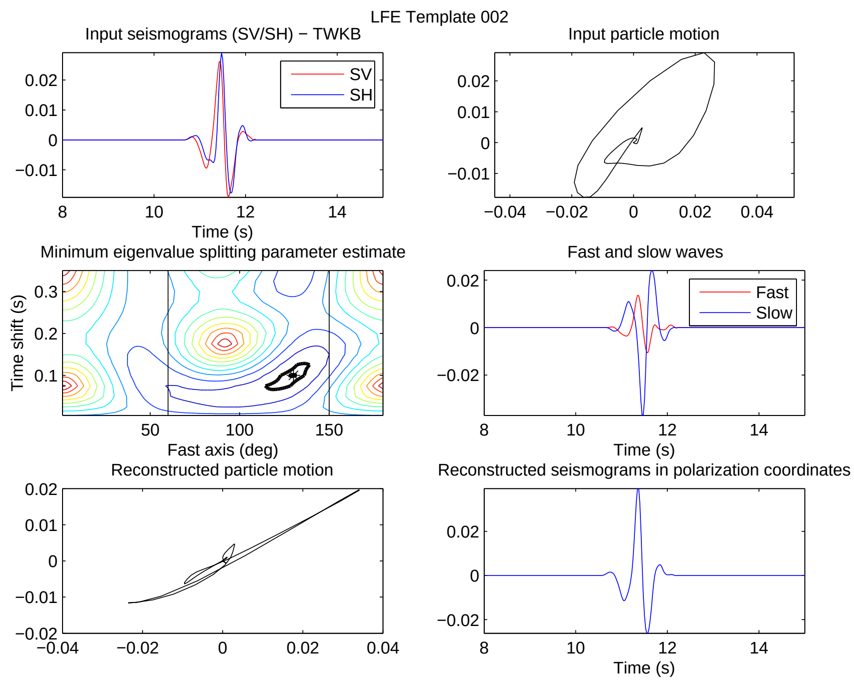

Figure 3.1: Stages of splitting analysis for LFE template 002. (a) Windowed and tapered SV-SH waveforms. (b) Elliptical particle motion indicative of anisotropic wave propagation. (c) Grid search to minimize second eigenvalue of the covariance matrix. Star represents minima, thick black lines represent confidence levels. Vertical black lines mark ϕ_0 and $\phi_0 + \pi/2$. (d) Fast and slow waves (e) Linearized particle motion of corrected seismograms. (f) Reconstruction of original isotropic waveform.

3.2 Results

A suite of 90 LFE templates representing a relatively uniform sampling of the tremor prone region are used to perform a splitting analysis over a group of 20 stations located on SVI (figure 2.3). The complete analysis leads to 517 valid splitting measurements out of a potential 1800 source-receiver pairs. Table 1 shows a summary of the resulting measurements at all stations. Due to the requirement of steeply incident arrivals, the use of certain stations becomes limited by the event distribution. Stations SNB, GOWB, SSIB and PFB are located outside of the region most densely populated with LFEs, which naturally leads to shallower incidence angles. Other stations with limited measurements, e.g. TWGB, are characterized by poor SNR or strong distortions in the original S-waveforms that make isolating arrivals difficult (e.g. figure 2.2). Station TWGB lies in close proximity to the surface trace of the San Juan Fault and atop potentially complex lithology, thus it is conceivable that this waveform distortion is a consequence of strong local anisotropy/heterogeneity. Stations TWBB and TSJB are located near TWGB and often display similar but less severe behaviour.

Table 3.1: Splitting parameters at stations employed in this study. Mean values and standard deviations for fast direction (ϕ) and split time (δt). Azimuthal distribution of ϕ uses directional statistics to compute means and standard deviations [5].

Station	Latitude	Longitude	$\delta t(s)$	$\pm\delta t(s)$	$\phi(^\circ)$	$\pm\phi(^\circ)$	N. Meas.
SSIB	48.7558	-123.3875	0.19	0.09	109	27	14
SNB	48.7751	-123.1723	0.21	0.08	95	37	3
GOWB	48.7369	-123.1848	0.16	0.06	121	34	5
SILB	48.6020	-123.2815	0.11	0.08	87	32	23
PGC	48.6500	-123.4500	0.10	0.04	111	32	30
KELB	48.6611	-123.5701	0.10	0.04	103	26	37
MGCB	48.6317	-123.6808	0.11	0.06	97	30	37
TWKB	48.6449	-123.7332	0.13	0.06	99	15	44
LZB	48.6117	-123.8236	0.13	0.05	99	23	46
TSJB	48.6013	-123.9885	0.21	0.06	79	22	38
TWBB	48.5846	-124.0920	0.20	0.07	91	26	26
TWGB	48.6076	-124.2559	0.16	0.07	93	35	14
PFB	48.5750	-124.4444	-	-	-	-	0
LCBC	48.4834	-124.2619	0.14	0.06	60	47	10
JRBC	48.3957	-123.9601	0.10	0.06	80	44	18
SOKB	48.3947	-123.6731	0.12	0.06	121	35	45
GLBC	48.3960	-123.6363	0.11	0.06	115	32	37
SHVB	48.4723	-123.3737	0.18	0.08	122	33	31
KHVB	48.5688	-123.4663	0.12	0.04	112	30	37
VGZ	48.4139	-123.3244	0.15	0.08	116	31	22

3.2.1 Initial polarization direction

We first analyze the distribution of initial polarization directions ϕ_0 and compare with source mechanism predictions. *Bostock and Christensen* [9] acquired ϕ_0 estimates using raw tremor waveforms and found ϕ_0 to be scattered but to average close to the NE directed plate motion direction, consistent with the interpretation of LFEs as resulting from shear failure at the plate boundary. Figure 3.2 shows a composite plot of ϕ_0 represented in rose histograms at individual station locations. Each histogram contains 50 bins of width 7.2°. In comparison to ϕ_0 from *Bostock and Christensen* [9], ϕ_0 from LFE template splitting measurements exhibit a similar but more tightly defined tendency for original polarization direction to coincide with plate motion direction [36].

We expand on this analysis by comparing measured ϕ_0 with predicted polarization directions for an isotropic 1D velocity model. We take an average representative moment tensor solution for LFEs on SVI [41] and compute the predicted far-field radiation pattern (inset figure 3.3). We find strong agreement between predicted and observed initial polarization directions. Figure 3.3 displays a single event example where both observed and predicted ϕ_0 at stations TWBB and TSJB display considerable deviation from the plate motion direction, but are directly explained by the expected radiation pattern. Figure 3.4 displays single station comparisons of ϕ_0 plotted at the LFE epicenters. Station TWKB demonstrates an ideal case with strong consistency in predicted and measured ϕ_0 over the majority of LFE locations. Agreement at TWBB is less consistent; whereas the main cluster of events originating from under the LRC still exhibit reasonable agreement, there is considerably more variability for distant sources. Recovery of ϕ_0 is less reliable for noisy template waveforms or where strong waveform distortions are observed. The overall agreement aids in verifying the methods used in this study.

3.2.2 Fast polarization direction

Whereas original polarization directions provide corroboration for a common thrust mechanism, fast polarization directions yield information related to anisotropy. Figure 3.5 displays rose histograms of fast polarization directions at station locations. For stations in close proximity to the LRC we note some similarity between the dominant fast direction and the attitude of the nearest bounding fault. Western stations on the POLARIS-BC line crossing mainland SVI show a general E-W fast direction. Stations to the southeast (KHVB, SHVB, VGZ, GLBC and SOKB) exhibit fast directions that are subparallel to the Survey Mountain Fault, which defines the eastern extent of the surface expression of the LRC.

Two recent crustal anisotropy studies in SVI also compiled measurements of fast polarization direction using alternative datasets. *Balfour et al.* [4] employ local crustal and intraslab earthquakes (distribution is similar but not identical to that for crustal/instraslab earthquakes displayed in in figure 2.3), whereas the study by *Bostock and Christensen* [9] measures splitting on raw tremor waveforms from ETS episodes in Cascadia. Since LFE templates are acquired through network correlation of tremor data, we expect similarity between LFE and tremor splitting measurements, with improved consistency due to precise source locations. An earlier crustal anisotropy study [15] measured average $\phi = 113°$ at PGC for shallow crustal events, exhibiting good correspondence with our result (Table 1).

As expected, fast directions in this study reveal good agreement with those derived from raw tremor at common stations [9], with a general E-W trend for stations in close proximity to the San Juan Fault (figure 3.5). Moreover, the LFE measurements extend spatial coverage to stations along the south-east coast of SVI. A comparison between our fast polarization directions and those of *Balfour et al.* [4] are displayed in figure 3.6; agreement is mixed and will be addressed in section 3.3.

Figure 3.6 presents splitting measurements as a function of azimuth and incidence angle. We note some degree of azimuthal variation in ϕ at select stations. Where present, azimuthal variations manifest as spatially coherent clusters of similar ϕ. Stations PGC, LZB and TWKB exhibit approximately E-W fast directions for south-western azimuths yet trend closer to NW-SE for south-eastern azimuths. At SOKB, ϕ is rotated counter-clockwise for events originating from eastern azimuths when compared to events to from the north-west. Similarity in azimuthal variations of ϕ between neighbouring stations suggest that these small scale variations are genuine indications of heterogeneous anisotropy. Two such examples include station pairs TWKB/LZB and KELB/PGC (figure 3.6).

3.2.3 Delay times

Delay times across all stations and events vary between 0.05 and 0.3 s, whereas mean values over all stations vary between 0.1 and 0.21 s. We do not observe any systematic variation in delay time with backazimuth (figure 3.6), with the possible exception of station TWKB. *Bostock and Christensen* [9] reported larger delay times corresponding to northerly azimuths with an average $\delta t = 0.22$ s, as opposed to an average $\delta t = 0.07$ s for events from south-western azimuths; we observe a similar but less definitive trend. Whereas we lack measurements from northerly azimuths, the northern most events display larger split times (> 0.2 s) and decrease for south-western azimuths, with delay times ranging between 0-0.2 s. Figure 3.7 displays histograms of depth normalized delay times ($\delta t'$) for an E-W line of stations. We observe an increase in average $\delta t'$ from east to west, with maximum values occurring at TSJB. The large variance within the histograms hint at a strongly heterogeneous strength of anisotropy. Measured delay times are generally larger than those of *Balfour et al.* [4] and will be addressed in later discussion.

Schistose rocks are known to cause splitting due to preferred mineral orientation [12, 17, 28], thus we chose to investigate the potential influence of lithology on splitting measurements by combining laboratory measurements of LRC rock samples with structural information available on the geometry of the LRC (section 4).

3.3 Comparison with a prior forearc study

We herein refer to *Balfour et al.* [4] as *BCDM* for brevity. We credit the somewhat complementary event distributions as the primary contributor to the discrepancies in splitting measurements between the two studies. LFE epicenters occur predominantly on mainland SVI and arrive with subvertical incidence angles, whereas *BCDM* epicenters tend to lie along the coasts and arrive with shallower incidence angles. Figure 2.3 is a representative display of the respective distributions. Shared raypaths between LFE and crustal/instraslab events exist, but are limited. The variable sampling of the crust could lead to inherent sampling bias in the average splitting measurements. In the presence of heterogeneous anisotropy, these differences become more difficult to verify and interpret. Sampling bias may explain why average ϕ from *BCDM* are consistently rotated clockwise relative to average ϕ determined in this study (figure 3.6). For example, stations LZB and TWKB show some azimuthal variation in ϕ but the abundance in E-W directed measurements means that certain measurements are not represented in the mean, an issue that is due to the sample distribution.

Where azimuthal variations in ϕ are observed, agreement with *BCDM* fast directions are improved for azimuths with similar LFE/*BCDM* earthquake epicenters (figure 3.6). Examples include south-western azimuths for TWKB and LZB, along with eastern azimuths at SOKB. Without a more comprehensive event-by-event comparison it is unclear whether the improved agreement is genuine and reflects shared sources anisotropy. Mean fast directions at stations SSIB, SNB, GOWB and SOKB show good agreement with *BCDM*, although the limited LFE template measurements at SNB and GOWB suggest that these particular agreements should be taken with caution.

Average split times at TWGB, TSJB and LZB are larger than those from *BCDM* (listed in figure 3.6), this is potentially explained by propagation through a medium with HTI symmetry. Maximal splitting is produced when the propagation direction is perpendicular to the symmetry axis [e.g. 9, 12, 17]. For N-S propagation, the subvertical raypaths of LFEs would produce near maximal splitting, whereas the shallower incidence of instraslab/crustal earthquakes could produce anisotropy of a smaller magnitude [9]. This difference can be significant and could explain the smaller split times recorded by *BCDM* despite the generally longer raypaths for crustal/instraslab events at these stations.

Differences in delay times for stations along the east coast are difficult to reconcile due to the variable behaviour between stations. We focus on a subset of LFE events east of a line of constant longitude -123.6731° (longitude of station SOKB), with comparable ray geometries to crustal/intraslab events used by *BCDM*. For this subset, PGC and KHVB have average delay times of 0.1 and 0.13 s respectively, both smaller than those observed by *BCDM* (PGC: 0.12 s, KHVB: 0.18 s). Conversely, stations SOKB, SHVB and VGZ have mean delay times greater than *BCDM*, retaining mean values listed in figure 3.6. Without more information on the contributing event distribution, it is difficult to ascertain what may cause the discrepancies. The variable length of raypaths for intraslab and shallower crustal earthquakes may cause variations, however, *BCDM* reported no systematic increase in delay time with depth. Measurements for the remaining stations are too scattered and few to draw meaningful comparisons. In general the splitting measurements for LFE templates and *BCDM* appear to reflect different sampling of a heterogeneous, anisotropic crust.

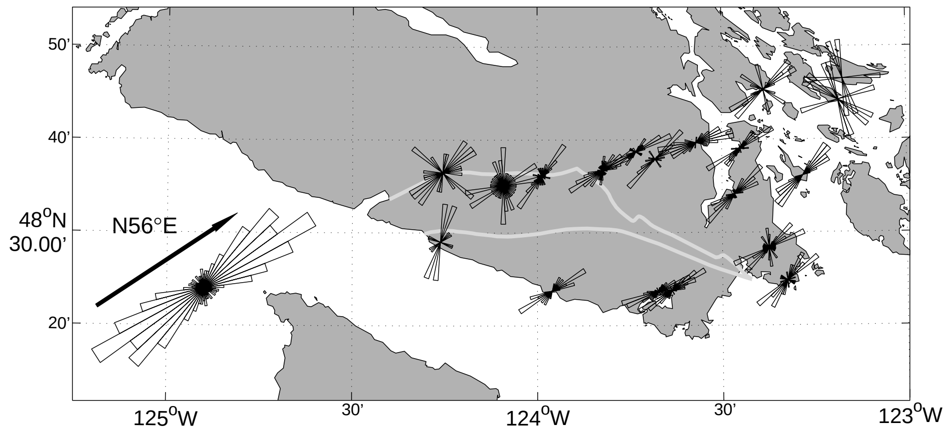

Figure 3.2: Rose histograms of original polarization direction ϕ_0 plotted at station locations. Cumulative rose histogram for all stations is shown at the lower left along with the local plate motion vector of the Juan de Fuca plate relative to the North American plate.

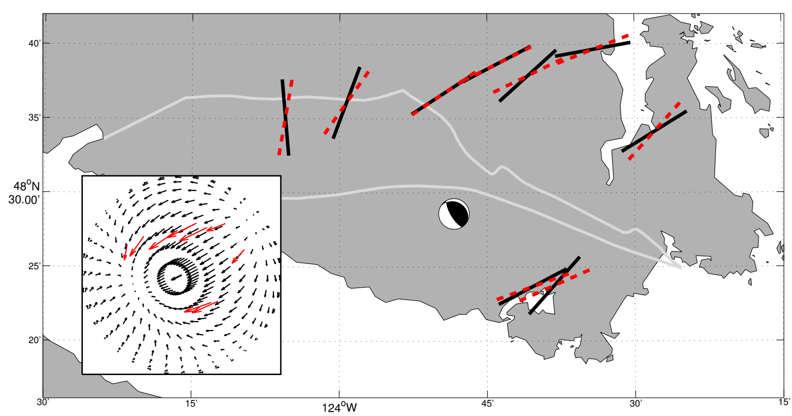

Figure 3.3: Single event comparison of observed (black lines) and predicted (dashed red lines) ϕ_0 plotted at station locations for LFE template 101. The representative LFE focal mechanism is plotted at the LFE epicenter. The corresponding radiation pattern is shown in the inset. Polarization vectors for predicted ϕ_0 are displayed as red arrows in the inset.

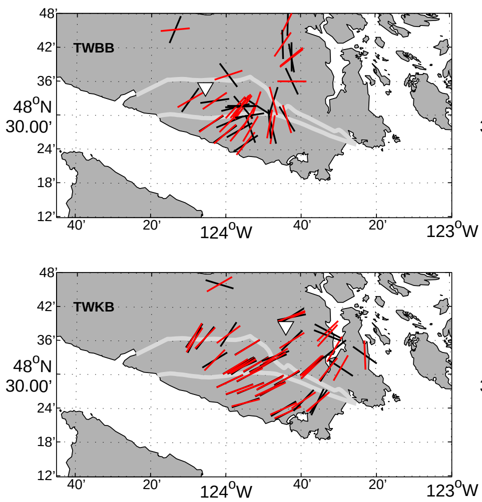

Figure 3.4: Single station comparisons for a range of POLARIS-BC stations displaying observed (black lines) and predicted (red lines) ϕ_0. ϕ_0 measurements are plotted at corresponding LFE epicenters.

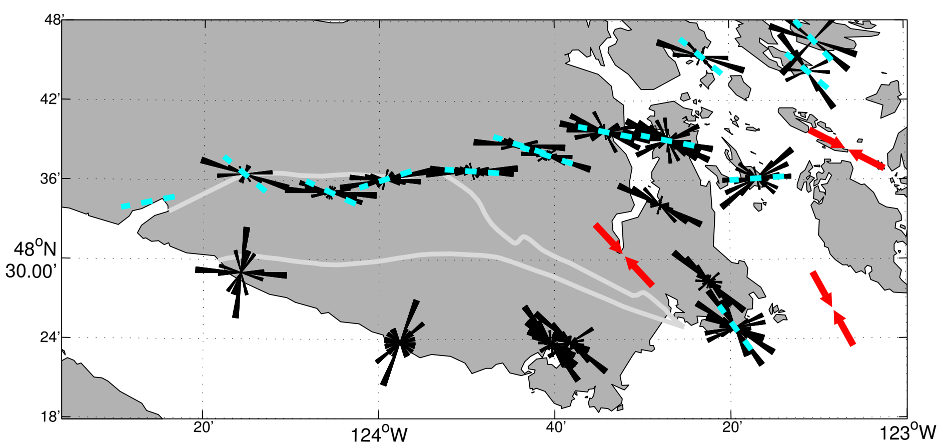

Figure 3.5: Rose histograms of fast polarization direction ϕ at station locations. Dashed cyan lines represent ϕ_{mode} for tremor splitting measurements [9]. Red arrows represent estimates of maximum horizontal compressive stress (σ_{Hmax}) [3].

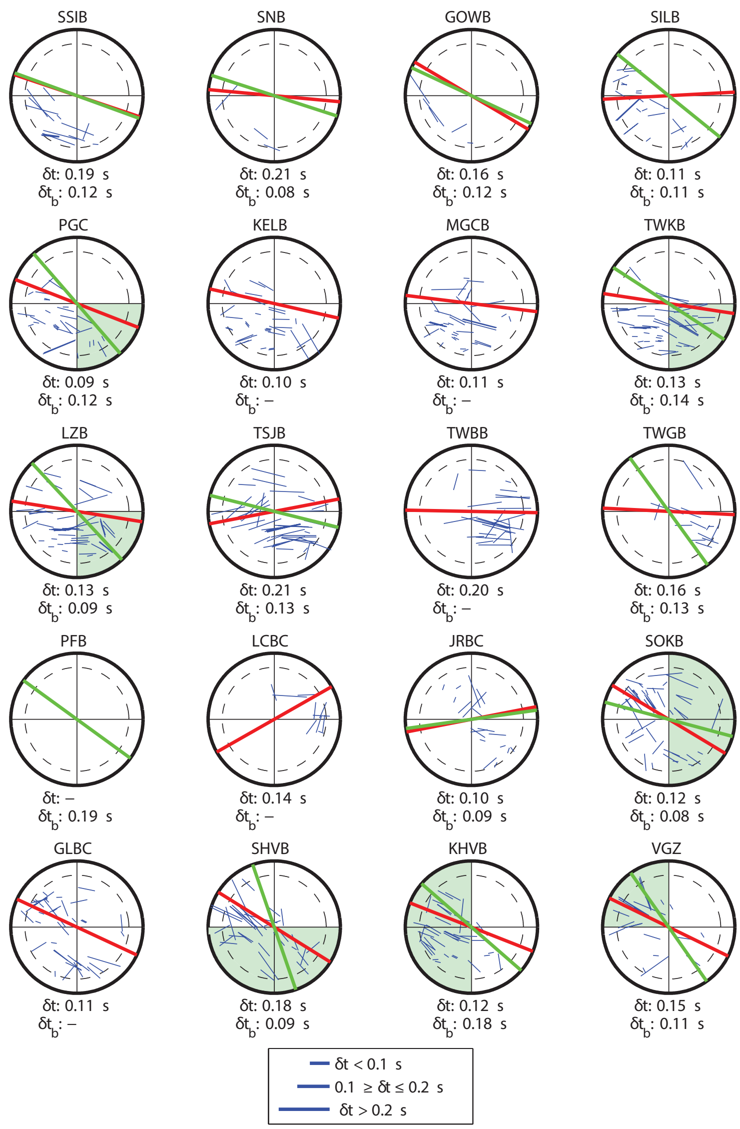

Figure 3.6: Equal area plots displaying δt and ϕ for all stations. Border represents 45° incidence angle and dashed line represents 35° incidence angle. ϕ are plotted as blue bars with lengths proportional to delay times. Mean ϕ from this study (red lines) and *Balfour et al.* [4] (green lines) are included for comparison. Mean delay times from this study (δt) and *Balfour et al.* [4] (δt_b) are also included. Shaded regions indicate backazimuths where LFEs are thought to share similar raypaths to crustal/instraslab events from *Balfour et al.* [4].

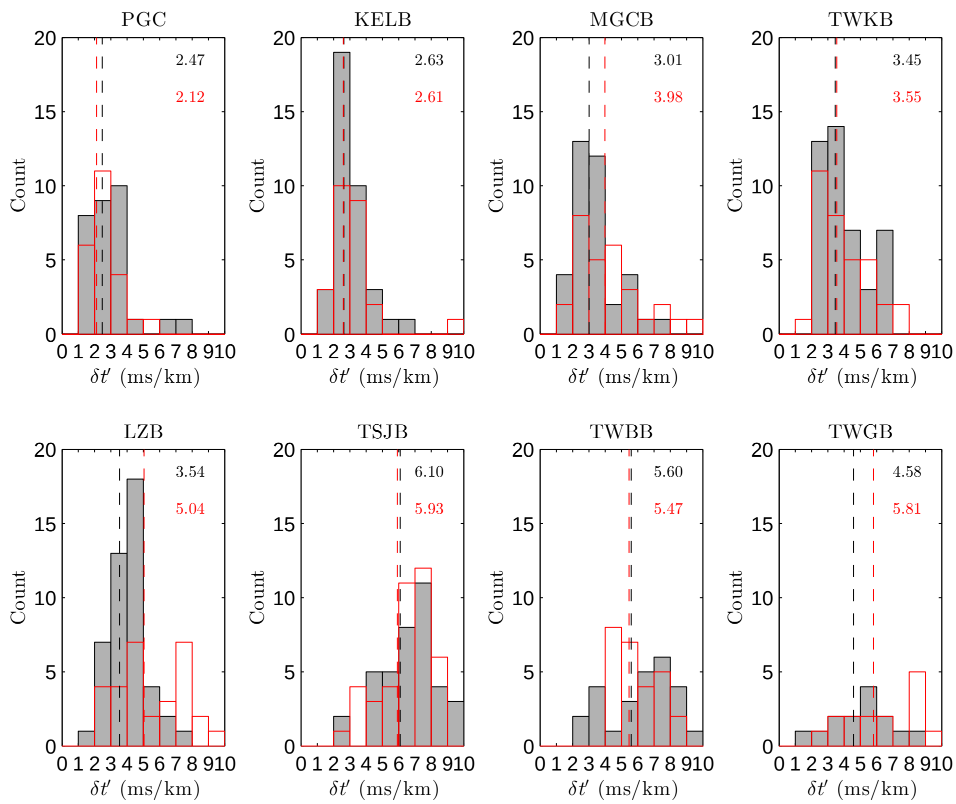

Figure 3.7: Histograms of depth normalized delay times ($\delta t'$) for E-W mainland stations. Grey histograms represent $\delta t'$ for LFE template measurements with mean values signified by a dashed black line. Mean value is listed in black in the top right. Histograms for synthetic $\delta t'$ computed with a subset of 50 LFEs, are shown as transparent bars with red outlines. Dashed red lines identify mean $\delta t'$ with numerical value listed in red.

Chapter 4

Forward Modeling

We seek to test the validity of the assertion that crustal anisotropy in SVI is primarily a result of mineral orientation in metamorphic rocks. We employ the spectral element method (SEM) to compute synthetic seismograms in 3D anisotropic models [33, 34]. SEM allows for accurate solutions to the full elastic wave equation with general anisotropy represented by 21 independent elastic constants. We develop a conceptually simple and geologically justifiable model that captures the systematic trends in ϕ, with less attention paid to precise matching of split times. Split times are dictated by both the extent and strength of anisotropic material, thus making detailed assumptions about either is problematic given the lack of information on their respective distributions.

4.1 Initial model and LFE source

We develop a regional mesh that encompasses the SVI region lying between 48.2°-48.8° latitude and $-123.0°$-$-124.75°$ longitude and translates to a region of approximately 130 km x 65 km in the E-W and N-S directions, respectively. The mesh extends to a depth of 50 km, enclosing the LFE distribution while maintaining a sufficient distance from the domain boundaries to mitigate the influence of boundary reflections. Absorbing boundary conditions are applied and a realistic topography and bathymetry model is used. We use a 3D P-wave velocity model [40] and compute S-wavespeeds using a constant V_p/V_s ratio of 1.76, an average value for continental crust [18]. Density is computed using a wavespeed-based empirical relation for crustal rocks [11]. We employ a purely isotropic background model upon which we superpose various anisotropic perturbation models. Two mesh doubling layers are implemented to maintain a similar number of grid points per wavelength throughout the mesh. The minimum period resolvable by the mesh is ∼0.6 s. Regional mesh is displayed in figure 4.1. Although LFE template waveforms display characteristic frequencies of 1-10 Hz, modeling was restricted to frequencies between 0.5-1.67 Hz, a decision that was dictated by considerations of numerical cost. To allow for comparisons between data and synthetics, we bandpass filter the data at frequencies resolvable by the mesh. Even within this bandpass LFE template waveforms retain a clearly defined arrival, thereby justifying our choice for a lower frequency band. It should be noted that we chose not to include the explicit signature of the (3-4 km) low velocity, high V_p/V_s zone that sits at the top of the subducting plate [30]. Any reflections/conversions therefrom should arrive as S-waves within the S-wave window with geometries similar to direct S. Hence they should not alter estimates of δt or ϕ. Due to the considerable similarity of LFE focal mechanisms over the entire suite of LFE events [41] we use a single representative moment tensor for all LFEs when conducting numerical simulations (figure 3.3).

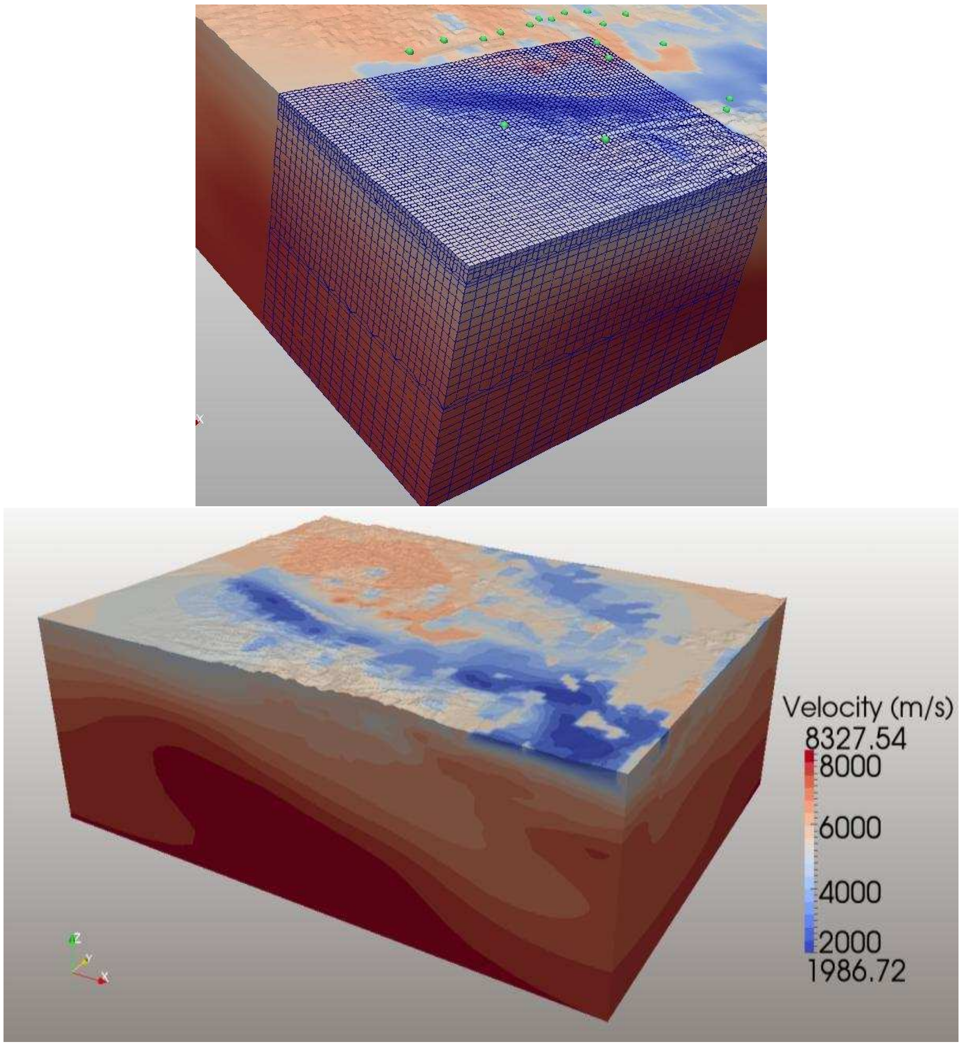

Figure 4.1: Images of regional mesh. Top: Mesh doubling structure is displayed with stations as green dots on the surface. Bottom: 3D tomographic V_p model used for modeling [40].

4.2 LRC anisotropy model

We expand upon the premise discussed in *Bostock and Christensen* [9] that crustal anisotropy in SVI is primarily a result of mineral orientation in the LRC. P-wave and S-wave velocities for a range of Leech River schist and phyllite samples demonstrate transverse isotropy with a symmetry axis perpendicular to their foliation and fast directions parallel to the foliation [9].

We first review prior constraints on geometry of the LRC. The surface expression of the LRC is bounded by three faults; the Leech River fault (LRF), San Juan fault (SJF) and the Survey Mountain fault (SMF) (figure 2.1). Seismic reflection surveys reveal the LRF and SMF to be thrust faults, dipping to the northeast at 35-45° to a depth of ∼10km [20, 29]. Subsequent reprocessing of select data [29] reveals an undulating LRF that begins as a steeply dipping (60°) fault near the surface and becomes shallowly dipping past 3 km depth. A lack of a reflection signature for the SJF was interpreted as indication of a steep northward dip of 60-70°. Reflection imaging off the west coast of SVI suggests that the LRF and SJF are both steeply dipping and merge at ∼13 km depth [21].

We implement azimuthal anisotropy by assuming that anisotropy can be represented as a transversely isotropic medium with the symmetry axis oriented in the horizontal plane (HTI). The appropriate elastic tensor is computed using velocity measurements for an LRC schist sample (L-4 schist sample from *Bostock and Christensen* [9]). The L-4 sample exhibits transverse isotropy with S-wave anisotropy of 11%, a relatively conservative value in comparison to other schistose rocks from the LRC that can exhibit S-wave anisotropy up to 30%. Orienting the symmetry axis within the horizontal plane equates to modeling a vertically dipping foliation as is prevalent in surface exposures of the LRC [27]. The two main adjustable parameters are the spatial extent of anisotropy and the orientation of symmetry axis in the horizontal plane. We test a range of models and present the preferred model.

4.3 Preferred model and results

A basic anisotropic model of a homogeneous block of HTI material with a symmetry axis oriented due north (E-W oriented foliation), is improved by iteratively increasing model complexity to reduce discrepancies between observed and synthetic ϕ. At the first iteration we alter the LRC spatial geometry following the constraints established in section 4.2. In later iterations we include differing anisotropic orientations.

In 4 iterations we reach a viable anisotropic model (figure 4.2 (a)). The LRF and SMF both dip shallowly at 30° to N35°E respectively; the preferred dip of these faults lie slightly below the lower estimates from reflection surveys [20]. The SJF dips steeply (70°) to the north and becomes shallower past 6 km to accommodate the interpretation that the SJF represents a listric thrust fault [20]. Projections of the dipping LRC bounding faults extend to 12 km depth and terminate forming a wedge of north/north-east trending material. Anisotropy in the model is divided into two distinct regions. In region 1, the symmetry axis is oriented due north and simulates a region of material with E-W trending foliation. Region 2 has foliation that is oriented subparallel to the strike of the SMF, with a symmetry axis oriented at ~N35°E. The inferred rock type in region 1 and 2 varies only in the orientation of the foliation.

We select a subset of 50 LFEs with ray geometries that encounter the anisotropic wedge model of the LRC to perform forward modeling. The synthetic data vary more systematically and the signature of the two distinct anisotropic regions is clearly observed (figure 4.2). We capture the general E-W fast direction trend for western POLARIS-BC stations, along with the transition to NW-SE fast directions for more easterly stations (e.g. TWKB, KHVB)(figure 4.2 (b)). While the aggregate behaviour is reasonably recovered, comparing the results for individual events/stations identifies deficiencies in the model.

Figure 3.7 includes the depth normalized delay times for the synthetic data in comparison to LFE template measurements, displaying fair overall agreement. The correspondence between trends of increasing average depth normalized delay times from east to west is notable and could further support LRC based anisotropy. Instances where split times are improperly matched can be observed through residuals, $r = \delta t_{obs} - \delta t_{syn}$ (figure 4.2(d-e)). Geographical clusters of slow ($r > 0$) or fast ($r < 0$) residuals are indicative of regions where anisotropy is too weak/strong along the corresponding raypaths. Fast residuals are prevalent at station LZB, which is reflected in the greater mean $\delta t'$ for synthetics (figure 3.7). TSJB displays both fast and slow residuals, overall agreement is strongest at TWKB. The deficiencies in the current model can be attributed to an imperfect model geometry that fails to capture complex lithology, particularly near the fault junction of the

SJF and SMF. *Fairchild and Cowan* [27] documented an increase in metamorphic grade from north to south from greenschist to amphibolite facies. Variable metamorphic grade (and consequently strength of anisotropy) is not reproduced in the current model, thereby presenting another potential source of error. With the current methods it is not possible to distinguish between the two sources of error.

Stations SOKB, GLBC and VGZ all show significant splitting with strong preferred directions for LFE template measurements, yet the current anisotropic model fails to reproduce splitting for synthetic seismograms (a single measurement at GLBC is the exception). The absence of a splitting signature is anticipated, as the corresponding LFE raypaths for these stations do not encounter the synthetic LRC anisotropy. Further adjustments, that honour prior geological constraints, could likely be made to improve agreement at stations VGZ and SHVB. This is not the case for other stations, where significant, implausible alterations would have to be made to account for anisotropy under an LRC model. The limited influence of the LRC suggests an alternate source of anisotropy exists along raypaths observed at SOKB, GLBC along with the trio of SSIB, SNB and GOWB.

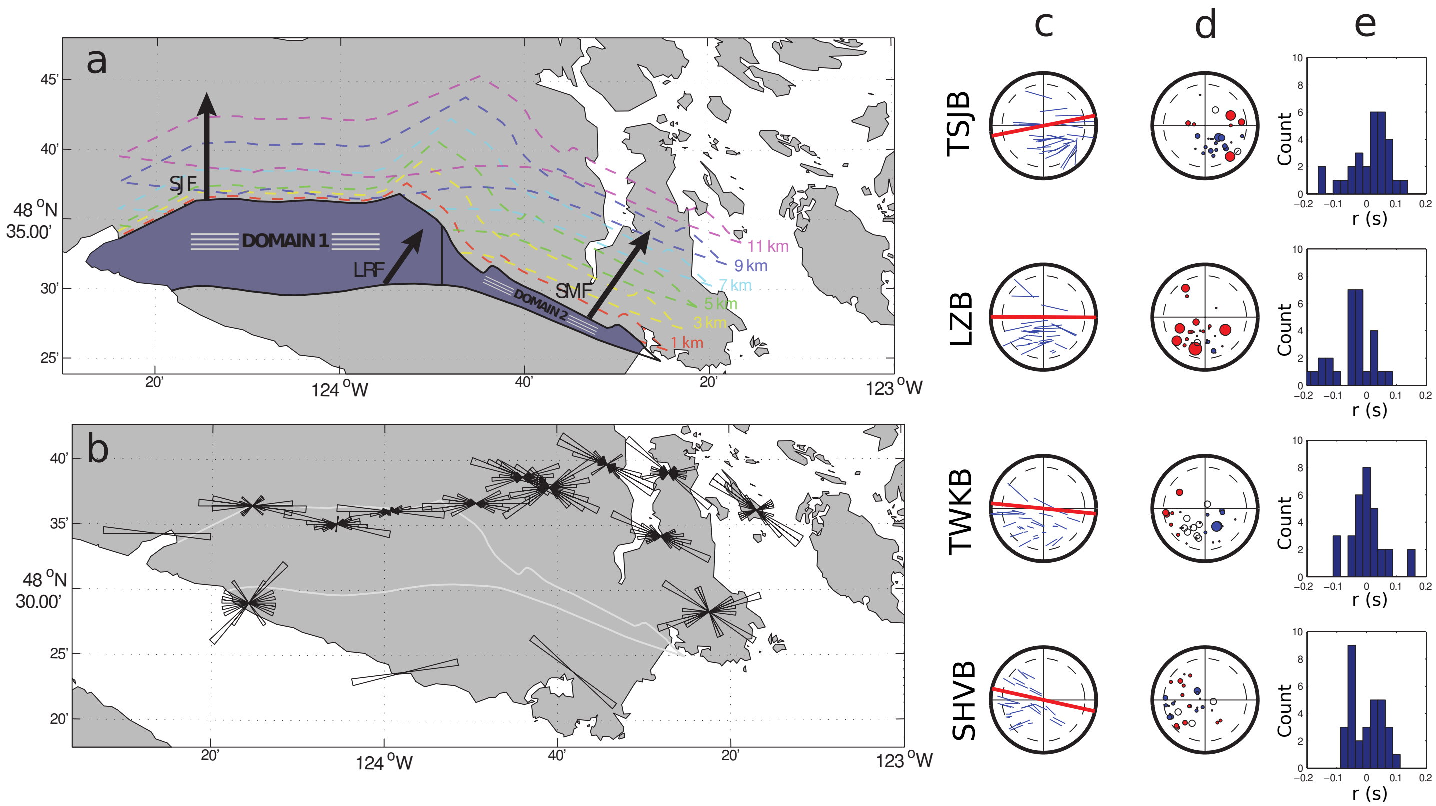

Figure 4.2: (a) Schematic diagram of LRC anisotropy model. Faults are labelled with dip directions indicated by black arrows. Anisotropic domains are labelled, light grey lines indicate orientation of vertically dipping foliation. Dashed lines represent projections of LRC at depth. (b) Rose histograms of synthetic fast polarizations, ϕ_{syn}. (c) Equal area plots displaying ϕ_{syn} at select stations, red line represents mean ϕ_{syn}. (d) Equal area plots showing azimuthal distribution of delay time residuals ($r = \delta t_{obs}$-δt_{syn}). Red and blue circles represent fast (r < 0) and slow (r > 0) residuals respectively, clear circles represent r=0. (e) Histograms of delay time residuals.

Chapter 5

Northern Washington

Although our focus in this thesis is to ascertain the nature of anisotropy below southern Vancouver Island, it will prove insightful in this respect to consider splitting measurements of LFE templates determined for stations immediately to the south below northern Washington state. LFE data for northern Washington were obtained using the same correlation methods used for SVI in section 2. For further details the reader is referred to [41]. We perform a splitting analysis, as outlined in section 3, for 100 LFE templates at 14 stations to produce 236 valid splitting measurements out of 1400 potential source-receiver pairs. Figure 5.1 displays rose histograms of ϕ at station locations along with equal area plots of ϕ for select stations. Splitting measurements are significantly less ordered and more complex than those on SVI. Mean delay times range from 0.1-0.15 s and are comparable in magnitude to delay times observed on SVI. Fast directions are scattered and exhibit significant variability in behaviour between neigbouring stations. Observations of ϕ for single stations exhibit variations with both azimuth and incidence angle (figure 5.1), stations W020 and GNW are two such examples. Station W020 displays near N-S ϕ at small incidence angles but trends closer to NE-SW for larger incidence angles. Azimuthal variations are somewhat consistent between neighbouring stations suggesting the variability is a genuine result of complex anisotropy. Complex anisotropy could be a consequence of highly deformed metamorphosed core rocks from the Olympic peninsula.

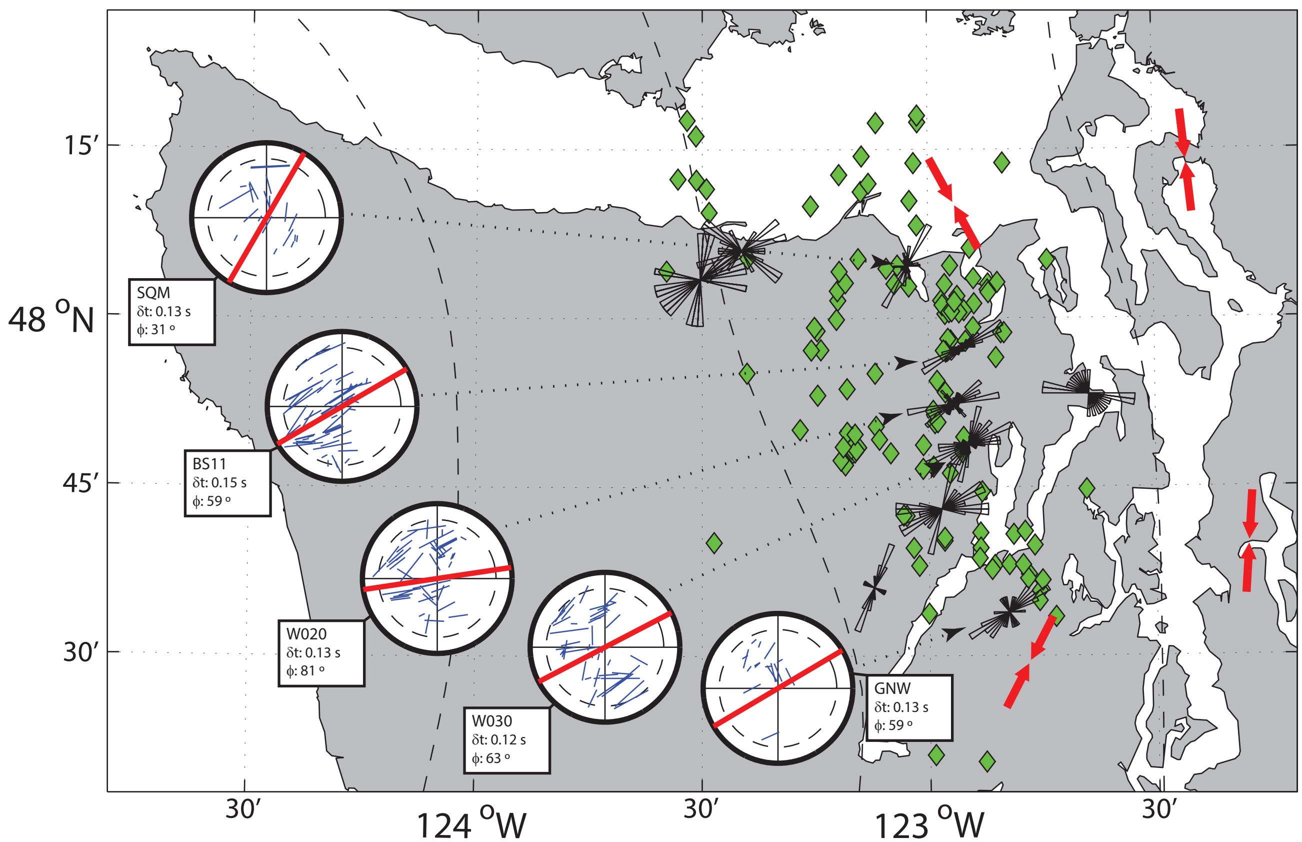

Figure 5.1: North Washington LFEs: Rose histograms of ϕ plotted at station locations. Green diamonds represent northern Washington LFE epicenters. Red arrows represent estimates of σ_{Hmax} from [3]. Equal area plots displaying ϕ are included for select stations. Red bars indicate ϕ_{mode}, ϕ_{mode} and mean δt are listed in boxes.

Chapter 6

Sources of Anisotropy

6.1 Extensive dilatancy anisotropy

Extensive dilatancy anisotropy is a concept where vertically-aligned fluid-filled cracks are oriented parallel or subparallel to the direction of maximum horizontal compressive stress (σ_{Hmax}), thus generating azimuthal anisotropy in crustal rocks. Prior studies [4, 15, 25] have interpreted anisotropy observed on SVI as due to extensive dilatancy anisotropy [23]. A stress inversion for northern Cascadia [3] provides stress estimates at two locations in close proximity to eastern stations on SVI (figure 3.5). Stations SHVB, VGZ, SOKB along with SSIB, SNB and GOWB to the north-east, have fast directions similar to the local σ_{Hmax}. The current anisotropic LRC model either lacks significant anisotropy along LFE raypaths to these stations or does not adequately reproduce observations of ϕ (figure 4.2). The similarity to σ_{Hmax} combined with inability for a wedge model of the LRC to account for anisotropy at these stations suggests that crack induced anisotropy could be the primary source of anisotropy observed at these stations.

σ_{Hmax} directions are generally considered to be margin-normal near the trench due to compression at the locked portion of the plate. To the east the subducting plate becomes weakly coupled and σ_{Hmax} becomes margin-parallel, in Cascadia this is thought to be due to the northward push of the Oregon block [36, 48, 49]. Under this stress model, we do not interpret anisotropy observed at POLARIS-BC stations on SVI to be related to crack anisotropy as dominant fast directions are almost perpendicular to the margin-parallel direction.

With increasing depth cracks are closed due to increasing lithostatic pressure; for anisotropy to persist at depth pore fluid pressures must be near lithostatic so that cracks remain open. V_p/V_s ratios of the continental crust overlying the subducting Juan de Fuca plate have been obtained through receiver functions of teleseismic body waves [2]. At SVI stations employed in this study, V_p/V_s varies between 1.59 and 1.83 with a mean of 1.73, slightly below the global average of 1.76 for continental crust [18]. The below average V_p/V_s ratios do not suggest elevated fluid pressures that would be required to prop open cracks. Electrical conductivity studies on SVI [46] have observed elevated conductivities below SVI at depths coincident with a seismically reflective layer [20] corresponding to the low S- velocity zone [1, 40]. The high conductivity region below SVI is interpreted as a region of trapped fluids within or above the subducting Juan de Fuca plate. However, electrical conductivities in the overlying crust of the North American plate are not elevated and do not suggest an abundance of fluid that would be required to elevate fluid pressures. A lack of fluids would be consistent with the interpretation of a sealed or low permeability plate boundary [1] that coincides with the ETS zone. Without elevated fluid pressures crack anisotropy would have a limited depth extent that is dependent on rock type and porosity [18].

σ_{Hmax} directions on northern Washington [3] are displayed in figure 5.1 and are generally N-S, trending near margin parallel. While some of the observed fast directions on northern Washington coincide with the local σ_{Hmax} directions (e.g. select azimuths at stations W020, W030 and GNW), the majority do not. The complex splitting patterns observed on northern Washington could be a result of multiple sources of anisotropy, that include crack induced anisotropy.

6.2 Mineral preferred orientation of the Leech River Complex

We assert that the anisotropy we observe on mainland SVI is primarily a result of the preferred mineral orientation of highly anisotropic rocks from the LRC. The geology of the LRC suggests a HTI model that adequately explains the observed splitting measurements. The LRC is mostly comprised of metamorphosed phyllites and schists that exhibit pervasive foliations with strong phyllosilcate lattice preferred orientations [22, 27]. Extensive structural analyses determined that two major deformational events have occurred in the tectonic history of the LRC, with the latter generating slaty cleavage and schistosity [27, 42]. Orientations of foliated planar folds produced by the second deformation are consistently steeply dipping and strike approximately east-west. The transversely isotropic LRC schists and phyllites [9] and observations of structural geology imply a source of azimuthal anisotropy generated by a HTI medium with a slow axis normal to the plane of foliation. The implementation of such a model in the forward modeling confirms the validity of an anisotropy model based upon preferred mineral orientation of the LRC.

E-W trending ϕ observed at mainland POLARIS-BC stations are consistent with the east-west striking foliation in the main body of the LRC. Geologic mapping suggests that the foliation trend rotates to the east, becoming subparallel to the strike of the SMF yet remains steeply/vertically dipping [35, 37]. By incorporating this change in dominant foliation direction in our forward model, we can recreate the NW-SE ϕ observed for some eastern stations using a north/north-east dipping wedge model that extends to 12 km. While the assumption that the foliation is vertically dipping throughout the LRC may not be valid, highly anisotropic LRC schists and phyllites (up to 30 % S-wave anisotropy) can generate up to 0.3 s splitting with a uniform thickness of as little as 2-3 km [9]. The trade-off between extent and strength of anisotropy allows for a shallower extent of vertically dipping foliation provided anisotropy is stronger; thereby supplying a more plausible alternative.

Assuming a constant strength of anisotropy in the LRC, the heterogeneous magnitude of anisotropy indicated by the increase in normalized delay times from east to west could be due to the lateral variations in the extent of the LRC. Normalized delay times from forward modeling display a similar trend but generally have more scattered delay times (figure 3.7). The synthetic wedge model is thickest below TSJB/TWBB/TWGB whereas to the east the dipping arm of the LRC is significantly thinner. An alternative explanation relates to fault zone mylonites as observed in the Brevard fault zone, a continental strike-slip/thrust fault. Above 200 MPa mylonitic metamorphic rocks of the fault zone were found to exhibit transverse isotropy due to preferred mineral orientation, which at lower pressures is enhanced by oriented cracks [19]. The presence of similar fault zone rocks in the bounding faults of the LRC may also explain why normalized delay times are increased for stations in close proximity to the faults. We also acknowledge that in the vicinity of fault zones crack anisotropy can be anomalously high, owing to large surface fractures [23]. Increased proximity of eastern stations to LRC fault zones presents another potential explanation for the E-W increase in normalized delay times.

The azimuthal variations observed at LZB and TWKB are reproduced by the two domain synthetic LRC model. Western azimuths record ϕ preferentially oriented E-W, whereas eastern azimuths tend towards NW-SE (figure 4.2). It is conceivable that anisotropy related to maximum horizontal compressive stress is a more slowly varying function of position in comparison to anisotropy due to mineral orientation, thus given the stress model established earlier we do not attribute the azimuthal variations in ϕ to local variations in σ_{Hmax}. We interpret spatial clusters of ϕ as an indication for heterogeneous anisotropy on SVI resulting from complex lithology with preferred mineral orientation that leads to small-scale azimuthal variations in ϕ.

6.3 Mineral preferred orientation of the Olympic Peninsula

The core rocks of the Olympic peninsula (figure 6.1) are comprised of two major accretionary terranes; western core rocks are non-slaty and locally coherent whereas the slaty eastern core rocks are pervasively sheared and exhibit well developed slaty-cleavage. The eastern core is predominantly composed of shale, sandstone and siltstone that have been variously metamorphosed to slate, semischist and phyllites. Core units form long irregular packets that vary between disrupted formations of sandstone/semischist with slate/phyllite to relatively intact interbedded sandstone and slate [47]. Whereas sandstone is seismically isotropic, velocity measurements on Olympic core slates indicate that they exhibit transverse isotropy. At 400 MPa, a sample of slate from Hurricane Ridge has $V_{qs1} = 3.79$ kms $^{-1}$ and $V_{qs2} = 2.94$ kms $^{-1}$ ($\sim$ 7% S-wave anisotropy) for propagation perpendicular to the symmetry axis. The interbedding of slate with sandstone acts to effectively dilute the anisotropy of the aggregate medium.

Structural analyses of the Olympic core rocks provide important clues about the origin and nature of crustal seismic anisotropy in SVI and northern Washington. Based on field observations of lineations, *Tabor and Cady* [47] have divided the Olympic Eastern core rocks into two major structural domains, with a boundary running approximately north-south. Slaty cleavages in the Western domain dip steeply to the east and northeast and the lineations plunge eastward. In the Eastern domain cleavages dip steeply o the west and southwest and lineations plunge westward. The orientations of slaty cleavage, bedding and axial planes of folds are nearly coplanar throughout both domains. Although structural details of the core rocks show considerable complexity, the provide a coherent model of slates with a fan of cleavage extending asymmetrically to the east with dips increasing to near vertical from west to east [47]. Of importance is the overall continuity of the slaty cleavage over distances of several kilometers, a condition that is favourable to generate observable seismic anisotropy.

Tomography [40] and reflection [20] studies have postulated that the Olympic core rocks are underthrust beneath the Eocene basalts of northern Washington and SVI as illustrated in the schematic diagrams in figure 6.1. Figure 6.1b presents an interpreted geologic profile along BB' based upon *Clowes et al.* [20] and includes reflectors imaged in the study. A dipping reflector beneath SVI was interpreted as the northward continuation of the Hurricane Ridge fault that is underlain by core rocks from the Olympic peninsula. The potential presence of anisotropic slate from the Olympic core beneath SVI presents a third source of anisotropy that could explain anisotropy for stations such as SOKB, GLBC, SSIB and others from SVI that we have not associated with the LRC. In addition, potential field studies beneath SVI identified a region of higher density (3140 kg/m^3) material underlying the Eocene basalts and LRC with a lower boundary defined by the E-layer [26]. This layer has been interpreted as either underplated metamorphosed fragments of the LRC/Eocene basalts or high density rocks resulting from metamorphosis of accreted sedimentary rocks. If the metamorphic rocks exhibit strong preferred mineral orientation they could represent a source of deep crustal anisotropy that has not been illustrated in figure 6.1.

Similarly, splitting observed on northern Washington may also be related to anisotropy from underlain Olympic slates as illustrated in figure 6.1c. Figure 6.1c is based upon P-wave tomographic profiles across northern Washington [40]. The variability of the terrane along with the mixed degrees of deformation may be the cause of the complex anisotropy displayed by variations of ϕ with azimuth and incidence angle. The Eocene basalts that overlay the core rocks on SVI and northern Washington are isotropic and do not influence observations of anisotropy [17]. Whereas the Hurricane Ridge slate exhibits relatively weak anisotropy in comparison to LRC phyllites and schists, the extent of the core rocks is believed to be significantly greater than that of LRC rocks. We believe the core rocks may extend as far as the plate boundary. Using the velocities stated earlier, Olympic slates could produce the 0.1-0.15 s of splitting typically observed in northern Washington with as little as 1-2 km for propagation perpendicular to the symmetry axis.

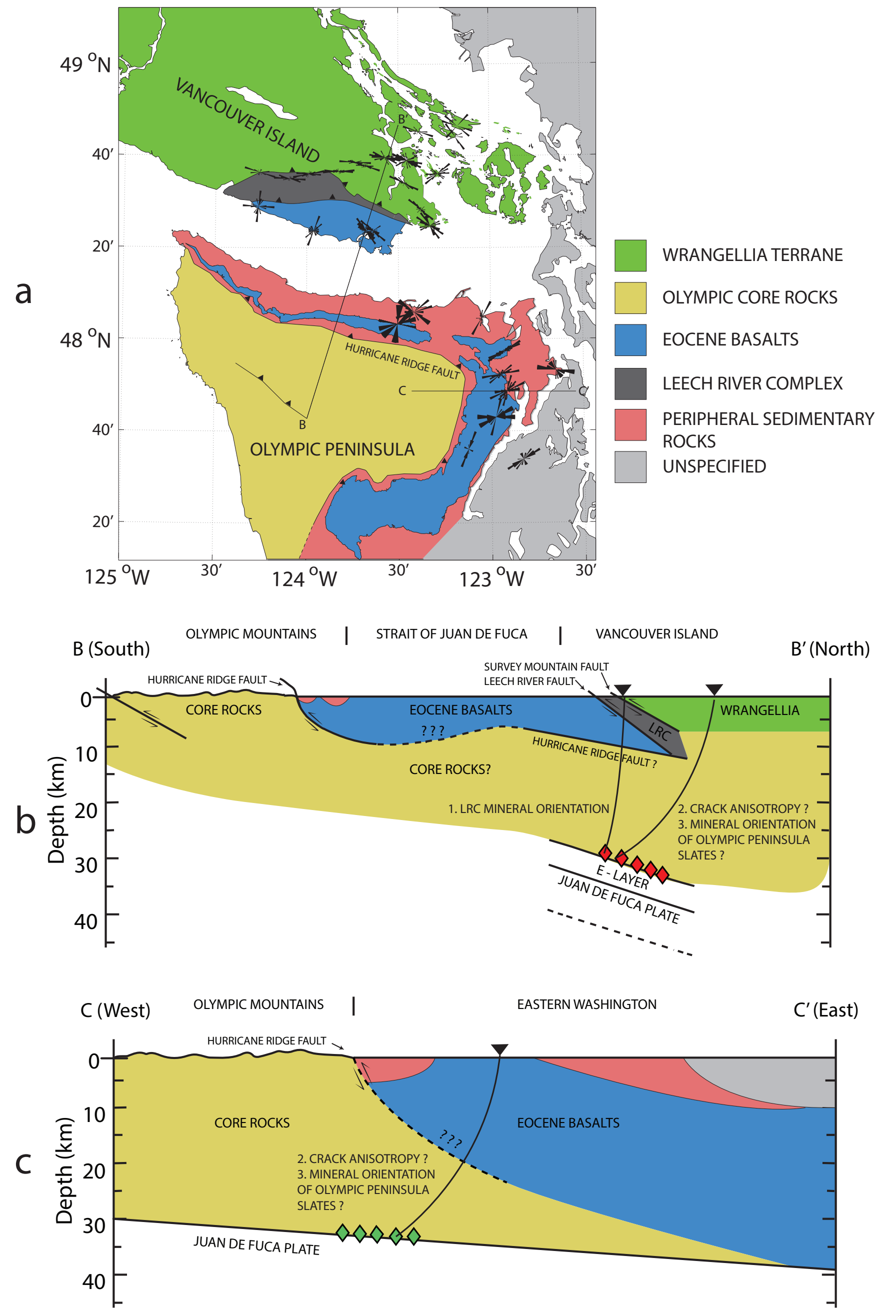

Figure 6.1: Schematic diagrams illustrating geological terrane and interpreted depth sections. (a) Major geological terranes of northern Cascadia with rose histograms of ϕ included. (b) Geologic interpretation of depth profile BB' based upon *Clowes et al.* [20]. Illustrates typical LFE paths and lists associated sources of anisotropy. (c) Geologic interpretation of depth profile CC' based upon *Ramachandran et al.* [40]. Illustrates underthrusting of Olympic core rocks beneath Eocene basalts.

Chapter 7

Summary

We have conducted a splitting analysis using LFE templates distributed on southern Vancouver island and northern Washington and presented the associated fast directions and delay times. Pervasively foliated and vertically dipping schists and phyllites in the Leech River Complex lead to anisotropy generated by a transversely isotropic medium with a symmetry axis in the horizontal plane. Anisotropy observed at the majority of mainland stations can be readily explained by anisotropy resulting from preferred mineral orientation of rocks within the Leech River Complex. Anisotropic forward modeling using a north/north-east dipping LRC wedge model that exhibits HTI symmetry was able to reproduce trends in dominant fast directions, normalized delay times and in select cases, azimuthal variations in fast direction. Crack anisotropy may provide an alternative explanation for anisotropy observed at stations that showed little relation to LRC properties; agreement with local estimates of maximum horizontal compressive stress was typically improved at these stations. Prior studies suggested that anisotropy observed at stations along SVI results from stress aligned cracks, thus making them candidates to monitor local stress patterns. We have demonstrated that anisotropy at the same stations is equally well explained by preferred mineral orientation of the Leech River Complex thereby casting doubt on prior conclusions. Splitting observations on northern Washington appear to be due to a mixture of crack anisotropy and the preferred mineral orientation of anisotropic slates of the Olympic core rocks that underthrust local terranes. We suggest that the anisotropic slates of the Olympic core may extend beneath southern Vancouver Island and present an additional source of anisotropy. If so, anisotropy due to the preferred mineral orientation of metamorphosed, accreted sedimentary rocks may be a global feature in forearc crusts of subduction zones.

Bibliography

[1] Audet, P., M. Bostock, N. Christensen, and S. Peacock (2009), Seismic evidence for overpressured subducted oceanic crust and megathrust fault sealing, *Nature*, *457*, 76–78.

[2] Audet, P., M. G. Bostock, D. C. Boyarko, M. R. Brudzinski, and R. M. Allen (2010), Slab morphology in the Cascadia fore arc and its relation to episodic tremor and slip, *J. Geophys. Res.*, *115*, B00A16, doi:10.1029/2008JB006053.

[3] Balfour, N. J., J. F. Cassidy, S. E. Dosso, and S. Mazzotti (2011), Mapping crustal stress and strain in southwest British Columbia, *J. Geophys. Res.*, *116*.

[4] Balfour, N. J., J. F. Cassidy, and S. E. Dosso (2012), Crustal anisotropy in the forearc of the northern Cascadia Subduction Zone, British Columbia, *Geophys. J. Int.*, *188*, 165–176, doi:10.1111/j.1365-246X.2011.05231.x.

[5] Berens, P. (2009), CircStat: A MATLAB Toolbox for Circular Statistics, *J. Stat. Soft.*, *31*, 1–21.

[6] Beroza, G. C., and S. Ide (2011), Slow earthquakes and nonvolcanic

tremor, *Annu. Rev. Earth Planet. Sci.*, *39*, 271–296, doi:10.1146/annurev-earth-040809-152531.

[7] Booth, D. C., and S. Crampin (1985), Shear-wave polarizations on a curved wavefront at an isotropic free surface, *Geophys. J. R. Astron. Soc.*, *83*, 31–45.

[8] Bostock, M. G. (2013), The Moho in subduction zones , *Tectonophysics*, *609*, 547 – 557, doi:http://dx.doi.org/10.1016/j.tecto.2012.07.007.

[9] Bostock, M. G., and N. I. Christensen (2012), Split from slip and schist: Crustal anisotropy beneath northern Cascadia from non-volcanic tremor, *J. Geophys. Res.*, *117*, B08303, doi:10.1029/2011JB009095.

[10] Bostock, M. G., A. A. Royer, E. H. Hearn, and S. M. Peacock (2012), Low frequency earthquakes below southern Vancouver Island, *Geochem., Geophys., Geosyst.*, *13*, doi:10.1029/2012GC004391.

[11] Brocher, T. M. (2005), Empirical relations between elastic wavespeeds and density in the Earth's crust, *Bull. Seis. Soc. Am.*, *95*, 2081–2092.

[12] Brocher, T. M., M. A. Fisher, E. L. Geist, and N. I. Christensen (1989), A high-resolution seismic reflection/refraction study of the Chugach-Peninsular Terrane Boundary, southern Alaska, *J. Geophys. Res.*, *94*, 4441–4455.

[13] Brown, J. R., G. C. Beroza, and D. R. Shelly (2008), An autocorrelation method to detect low frequency earthquakes within tremor, *Geophys. Res. Lett.*, *35*, doi:10.1029/2008GL034560.

[14] Brown, J. R., G. C. Beroza, S. Ide, K. Ohta, D. R. Shelly, S. Y. Schwartz, W. Rabbel, M. Thorwart, and H. Kao (2009), Deep low-frequency earthquakes in tremor localize to the plate interface in multiple subduction zones, *Geophys. Res. Lett.*, *36*, doi:10.1029/2009GL040027.

[15] Cassidy, J. F., and M. G. Bostock (1996), Shear-wave splitting above the subducting Juan de Fuca Plate, *Geophys. Res. Lett.*, *23*, 941–944.

[16] Christensen, N. I. (1965), Compressional wave velocities in metamorphic rocks at pressures to 10 kilobars, *J. Geophys. Res.*, *70*, 6147–6164.

[17] Christensen, N. I. (1966), Shear wave velocities in metamorphic rocks at pressures to 10 kilobars, *J. Geophys. Res.*, *71*, 3549–3556.

[18] Christensen, N. I. (1996), Poisson's ratio and crustal seismology, *J. Geophys. Res.*, *101*, 3139–3156.

[19] Christensen, N. I., and D. Szymanski (1988), Origin of reflections from the Brevard Fault zone, *J. Geophys. Res.*, *93*, 1087–1102.

[20] Clowes, R. M., M. T. Brandon, A. G. Green, C. J. Yorath, A. S. Brown, E. R. Kanasewich, and C. Spencer (1987a), LITHOPROBE southern Vancouver Island: Cenozoic subduction complex imaged by deep seismic reflections, *Can. J. Earth Sci.*, *24*, 31–51.

[21] Clowes, R. M., C. Yorath, and R. Hyndman (1987b), Reflection mapping across the convergent margin of western Canada, *Geophys. J. of the R. Astron. Soc.*, *89*, 79–84.

[22] Cowan, D. S. (2003), Revisiting the Baranof Leech River hypothesis for early Tertiary coastwise transport of the Chugach Prince William terrane, *Earth and Planet. Sci. Lett.*, *213*, 463 – 475.

[23] Crampin, S. (1994), The fracture criticality of crustal rocks, *Geophys. J. Int.*, *118*, 428–438.

[24] Crampin, S., and S. Peacock (2005), A review of shear-wave splitting in the compliant crack-critical anisotropic earth, *Wav. Motion*, *41*, 59 – 77.

[25] Currie, C. A., J. F. Cassidy, and R. D. Hyndman (2001), A regional study of shear wave splitting above the Cascadia Subduction Zone: Margin-parallel crustal stress, *Geophys. Res. Lett.*, *28*, 659–662.

[26] Dehler, S., and R. Clowes (1992), Integrated geophysical modelling of terranes and other structural features along the western Canadian margin, *Can. J. Earth Sci.*, *29*, 1492–1508.

[27] Fairchild, L., and D. Cowan (1982), Structure, petrology, and tectonic history of the Leech River complex northwest of Victoria, Vancouver, *Can. J. Earth Sci.*, *19*, 1817–1835.

[28] Godfrey, N. J., N. I. Christensen, and D. A. Okaya (2000), Anisotropy of schists: Contribution of crustal anisotropy to active source seismic experiments and shear wave splitting observations, *J. Geophys. Res.*, *105*, 27,991–28,007.

[29] Green, A., B. Milkereit, L. Mayrand, C. Spencer, R. Kurtz, and R. M.

Clowes (1987), Lithoprobe seismic reflection profiling across vancouver island: results from reprocessing, *Geophys. J. Int.*, *89*, 85–90, doi:10.1111/j.1365-246X.1987.tb04392.x.

[30] Hansen, R. T., M. G. Bostock, and N. I. Christensen (2012), Nature of the low velocity zone in Cascadia from receiver function waveform inversion, *Earth and Planet. Sci. Lett.*, *337338*, 25 – 38, doi:http://dx.doi.org/10.1016/j.epsl.2012.05.031.

[31] Ide, S., D. R. Shelly, and G. C. Beroza (2007), Mechanism of deep low frequency earthquakes: Further evidence that deep non-volcanic tremor is generated by shear slip on the plate interface, *Geophys. Res. Lett.*, *34*, doi:10.1029/2006GL028890.

[32] Kennett, B. L. N. (1991), The removal of free surface interactions from three-component seismograms, *Geophys. J. Int.*, *104*, 153–154, doi:10.1111/j.1365-246X.1991.tb02501.x.

[33] Komatitsch, D., and J. Tromp (1999), Introduction to the spectral element method for three-dimensional seismic wave propagation, *Geophys. J. Int.*, *139*, 806–822, doi:10.1046/j.1365-246x.1999.00967.x.

[34] Komatitsch, D., C. Barnes, and J. Tromp (2000), Simulation of anisotropic wave propagation based upon a spectral element method, *Geophys.*, *65*, 1251–1260, doi:10.1190/1.1444816.

[35] Mayrand, L. J., A. G. Green, and B. Milkereit (1987), A quantitative approach to bedrock velocity resolution and precision: The Lithoprobe Vancouver Island Experiment, *J. Geophys. Res.*, *92*, 4837–4845.

[36] McCaffrey, R., R. W. King, S. J. Payne, and M. Lancaster (2013), Active tectonics of northwestern U.S. inferred from GPS-derived surface velocities, *J. Geophys. Res.*, *118*, doi:1029/2012JB009473.

[37] Muller, J. (1983), Geology, Victoria, Map 1553A, scale 1:100000 , geol. Surv. of Can.,Ottawa, Ont., Can.

[38] Nishide, N., T. Hashimoto, J. Funasaki, H. Nakazawa, M. Oka, H. Ueno, N. Yamada, I. Sasakawa, K. Maeda, K. Sugimoto, and T. Takashima (2000), Nationwide activity of low-frequency earthquakes in the lower crust in Japan, abstract Sk-P002 presented at Japan Earth and Planetary Science Joint Meeting, Geod. Soc. of Jpn., Tokyo.

[39] Nowack, R. L., and M. G. Bostock (2013), Scattered waves from low-frequency earthquakes and plate boundary structure in northern Cascadia, *Geophys. Res. Lett.*, *40*, 4238–4243, doi:10.1002/grl.50826.

[40] Ramachandran, K., R. D. Hyndman, and T. M. Brocher (2006), Regional p wave velocity structure of the northern Cascadia subduction zone, *J. Geophys. Res.*, *111*, B12301, doi:10.1029/2005JB004108.

[41] Royer, A., and M. Bostock (2013), A comparative study of low frequency earthquake templates in northern Cascadia, *Earth and Planetary Science Lett.*, doi:http://dx.doi.org/10.1016/j.epsl.2013.08.040, in press.

[42] Rusmore, M. E., and D. S. Cowan (1985), JurassicCretaceous rock units along the southern edge of the Wrangellia terrane on Vancouver Island, *Can. J. Earth Sci.*, *22*, 1223–1232.

[43] Shelly, D. R., G. C. Beroza, S. Ide, and S. Nakamura (2006), Low-frequency earthquakes in Shikoku, Japan, and their relationship to episodic tremor and slip, *Nature*, *442*, 188–191.

[44] Shelly, D. R., G. C. Beroza, and S. Ide (2007), Non-volcanic tremor and low-frequency earthquake swarms, *Nature*, *446*, 305–307.

[45] Silver, P. G., and W. W. Chan (1991), Shear wave splitting and sub-continental mantle deformation, *J. Geophys. Res.*, *96*, 16,429–16,454.

[46] Soyer, W., and M. Unsworth (2006), Deep electrical structure of the northern Cascadia (British Columbia, Canada) subduction zone: Implications for the distribution of fluids, *Geology*, *34*, 53–56, doi: 10.1130/G21951.1.

[47] Tabor, R. W., and W. M. Cady (1978), The structure of the olympic mountains, washington; analysis of a subduction zone, *USGS Professional Paper*, *1033*.

[48] Wang, K., T. Mulder, G. C. Rogers, and R. D. Hyndman (1995), Case for very low coupling stress on the cascadia ssubduction fault, *J. Geophys. Res.*, *100*, 12,907–12,918.

[49] Wells, R. E., and R. W. Simpson (2001), Northward migration of the cascadia forearc in the northwestern u.s. and implications for subduction deformation, *Earth Planets Space*, *53*, 275 – 283.